JGR Oceans

RESEARCH ARTICLE
10.1029/2024JC022051

Heterogeneous Mixing Processes Observed in the Dotson Ice Shelf Outflow, Antarctica

Tiago S. Dotto[1,2], Peter M. F. Sheehan[1], Yixi Zheng[1], Rob A. Hall[1], Gillian M. Damerell[1,3], and Karen J. Heywood[1]

[1]Centre for Ocean and Atmospheric Sciences, School of Environmental Sciences, University of East Anglia, Norwich, UK, [2]Now at National Oceanography Centre, Southampton, UK, [3]Now at Geophysical Institute, University of Bergen and the Bjerknes Centre for Climate Research, Bergen, Norway

Key Points:

- Elevated turbulent kinetic energy dissipation rates were found near the seabed and at mid-depths in the DIS outflow region
- Overturning instabilities associated with the outflow current result in strong turbulent mixing in middepth layers
- The two patterns of turbulent mixing produce large heat and salt fluxes to the upper layers

Supporting Information:

Supporting Information may be found in the online version of this article.

Correspondence to:

T. S. Dotto,
tiago.dotto@noc.ac.uk

Citation:

Dotto, T. S., Sheehan, P. M. F., Zheng, Y., Hall, R. A., Damerell, G. M., & Heywood, K. J. (2025). Heterogeneous mixing processes observed in the Dotson Ice Shelf outflow, Antarctica. *Journal of Geophysical Research: Oceans*, *130*, e2024JC022051. https://doi.org/10.1029/2024JC022051

Received 29 OCT 2024
Accepted 9 MAY 2025

Author Contributions:

Conceptualization: Tiago S. Dotto
Data curation: Karen J. Heywood
Formal analysis: Tiago S. Dotto
Funding acquisition: Rob A. Hall, Karen J. Heywood
Investigation: Tiago S. Dotto, Rob A. Hall
Methodology: Tiago S. Dotto, Peter M. F. Sheehan, Yixi Zheng, Gillian M. Damerell
Resources: Rob A. Hall, Karen J. Heywood
Supervision: Rob A. Hall, Karen J. Heywood
Visualization: Tiago S. Dotto
Writing – original draft: Tiago S. Dotto
Writing – review & editing: Tiago S. Dotto, Peter M. F. Sheehan, Yixi Zheng,

Abstract We present the first observations of ocean turbulent mixing rate in front of the Dotson Ice Shelf, where meltwater-enriched water leaves the cavity. The observations showed elevated turbulent kinetic energy dissipation rates (ε; $\sim 10^{-7}$ W kg^{-1}) and turbulent diapycnal diffusivities (κ; $\sim 10^{-2}$ m^2 s^{-1}) near the seabed and in middepth layers, which are three orders of magnitude above background values away from the outflow. Elevated diapycnal fluxes of heat and salt were observed in regions of high mixing, moving vertically on average O $\sim$ 10 W m^{-2} and O $\sim 10^{-6}$ kg m^{-2} s^{-1}, respectively, toward shallow depths. At middepth layers, the overturning instabilities are characterized by shear-driven symmetric and centrifugal instabilities. Our observations provide an understanding of mixing in front of fast-melting ice shelves and are key to developing better parameterizations and representations of mixing in climate models.

Plain Language Summary We conducted observations of turbulent ocean mixing in front of the fast-melting Dotson Ice Shelf. Elevated mixing was found at the outflow, where strong, relatively warm and fresh currents leave the ice shelf cavity. The proximity and friction of these currents with the local bathymetry were found to cause instabilities, which can generate strong vertical heat and salt transport toward shallow depths. These new observations can help us better represent polar turbulent mixing processes in climate models.

1. Introduction

The glaciers and ice sheets of Antarctica, where they reach the ocean, detach from the bedrock and float out over the water to form vast ice shelves, the basal melting of which is the largest contributor to Antarctic ice-mass loss (Depoorter et al., 2013; Greene et al., 2022; Rignot et al., 2019). This ice-mass loss releases large volumes of fresh glacial meltwater into the polar ocean and thus influences hydrography, circulation and deep-water formation (Silvano et al., 2018; Thompson et al., 2020). In addition to meltwater, ice shelf mass loss releases ecologically important trace metals such as iron and manganese into the oceans (van Manen et al., 2022), as well as sedimentary particles from within the ice shelf that contribute to phytoplankton blooms (Dinniman et al., 2020; Sherrell et al., 2015). Moreover, ice shelf meltwater can mix with warmer waters found beneath the ice shelf, and form a water mass which can be sufficiently buoyant to move to the upper ocean once it exits the ice shelf cavity, but still warm enough to contribute to sea ice thinning near ice shelf margins (Jourdain et al., 2017).

The depth and density at which these various products of ice shelf melting equilibrate in the ocean are vital to understanding their subsequent transport pathways and influence—and this depth is likely strongly influenced by the magnitude and distribution of turbulent ocean mixing in the vicinity of outflow currents from ice shelf cavities (Naveira Garabato et al., 2017). Turbulent mixing modifies water mass properties and is key to the transport and distribution of heat, salt, and other dissolved tracers between ocean layers. In Antarctica's shelf seas, quantifying turbulent mixing, and identifying the processes that drive it, is crucial to understanding and correctly modeling the effects of accelerating ice-mass loss in a warming climate.

Turbulent mixing is highly variable in space and time and is driven by a variety of processes, including mechanical stirring and destabilizing buoyancy forces. Mixing is generally elevated above rough bottom topography, often attributed to the breaking of internal waves (de Lavergne et al., 2016; Polzin et al., 1997). Mixing can also be elevated in the ocean interior in the presence of instabilities associated with density inversions and current shear, such as near fast-melting ice shelves and the buoyant, meltwater-rich outflows that emanate from their cavities (e.g., Arnscheidt et al., 2021; Naveira Garabato et al., 2017). In situ measurements of mixing in polar oceans are

Rob A. Hall, Gillian M. Damerell, Karen J. Heywood

still sparse, which hampers understanding of the main processes driving mixing near specific ice shelves and, thus, whether the characteristics of each region (e.g., local stratification, the volume of meltwater discharge, and the geometry of the ice draft) impact the magnitude of turbulence locally. Given the scarcity of observations, identifying the variety of processes responsible for mixing, accounting for their occurrence, and quantifying their impact, has not yet been possible. Although previous work has highlighted key processes by individual ice shelves (e.g., Naveria Garabato et al., 2017), the heterogeneity of mixing, and the diversity of its driving processes, is such that, absent further observations, the general applicability of existing case studies must be uncertain.

Here, we characterize and investigate the effects on vertical heat and salt fluxes associated with turbulent mixing processes in the outflow region of the Dotson Ice Shelf (DIS; Figure 1a), and compare the mixing patterns in front of it with observations from other Antarctic regions to assess similarities across ice shelves. This comparison will help refine our understanding of regional mixing processes and inform the design of future targeted field campaigns. The DIS is a fast-melting ice shelf, and together with its tributaries, it accounts for one-fourth of the current total ice mass loss in the Amundsen Sea (Milillo et al., 2022; Rignot et al., 2019). The mass loss of the DIS is dominated by ocean-driven basal melt (Jenkins et al., 2018). Relatively warm modified Circumpolar Deep Water (mCDW) enters predominantly on the eastern side of the DIS cavity near the seabed and melts the ice shelf from below (Yang et al., 2022). Basal melting is higher on the western side of the DIS, where a subglacial channel steers the freshened, buoyant flow north toward the ice front, melting the ice base further (Gourmelen et al., 2017; Wåhlin et al., 2024). The western DIS is characterized by an outflow leaving the cavity and exporting warm and meltwater-rich glacially modified water (Figure 1b; Miles et al., 2016; Randall-Goodwin et al., 2015). We show that the outflow is affected by the shallow seabed and vertical current shear in front of the cavity, resulting in elevated turbulent mixing locally, which increases the vertical fluxes of heat, salt, and potentially dissolved tracers to shallow depths.

2. Data and Methods

2.1. Hydrographic Data

A Rockland Scientific International Vertical Microstructure Profiler (VMP) 2000 was used to measure turbulent shear, conductivity, temperature and pressure at 76 hydrographic stations, split into 4 transects immediately north of the western DIS front (Figure 1b) between the 22nd January and 6th February 2022. During each transect, the VMP was deployed continuously profiling up and down between the sea surface and ~10–50 m above the seabed behind the slowly moving (~0.5 m s^{-1}) ship. Shear microstructure was measured at 512 Hz on the descent, whereas temperature, conductivity, and pressure were measured at 64 Hz on the descent and ascent casts. The shear microstructure data were processed using Rockland's ODAS software v3.2, and the profiles were averaged into 2-m bins. Temperature and salinity were 10-m smoothed with a Gaussian window to remove high-frequency signals to ensure that both down- and upcasts represent features of the same length scale regardless of small differences in data quality. We evaluate the remaining small differences between down- and upcasts at each station and confirm that these do not make a difference to our results. Here, we focused on layers below ~50 m depth because the VMP needs to be at a constant optimal falling speed of ~0.5–0.6 m s^{-1}, which was reached usually around that depth.

A 75-kHz RD Instruments shipboard Acoustic Doppler Current Profiler (SADCP) was used to measure horizontal water velocities. The velocity measurements were processed by the University of Hawaii Data Acquisition System onboard, using 5-min averages and were 16-m bin-averaged in the vertical (Hummon & Firing, 2003). The instrument provided good data down to 350 m water depth. The large-scale hydrographic context is given by conductivity-temperature-depth (CTD) and lowered acoustic Doppler current profiler (LADCP) measurements (Figure 1). The CTD sensors were calibrated post-cruise and the data were 2-m bin-averaged vertically.

Conservative temperature (Θ), absolute salinity (S_A), and Brunt-Väisälä frequency (N^2) were computed using TEOS-10 package for Matlab (McDougall & Barker, 2011). Neutral density (γ^n; Jackett & McDougall, 1997) was calculated with pre-TEOS-10 software. Upward-looking and downward-looking LADCP measurements were processed using the LDEO_IX toolbox using SADCP, CTD/GPS and bottom-track as constraints (Thurnherr, 2021). The LADCP data set has 8-m vertical bins. Tides were removed from the SADCP and LADCP current velocities using an updated version of the CATS2008 Antarctic tide model (Padman et al., 2002).

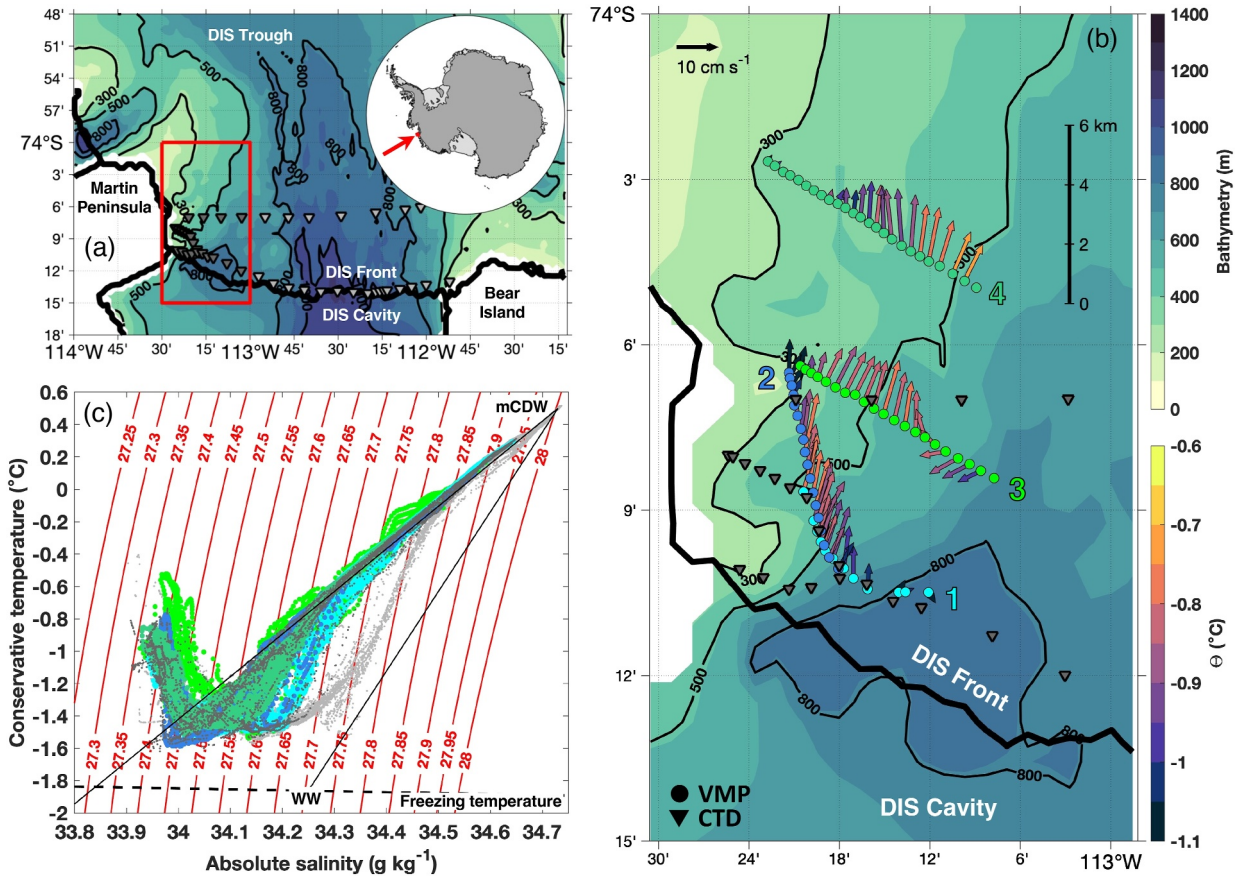

Figure 1. (a) Study region and CTD stations conducted at the Dotson Ice Shelf (DIS) front. Bathymetry from BedMachine Antarctica v3 (Morlighem et al., 2020), colorbar is shown in panel (b). Inset shows the study region. The red rectangle outlines the study area shown in panel (b). Dark gray triangles are CTDs conducted west of 113°W, and light gray triangles are CTDs conducted east of 113°W. (b) Vertical Microstructure Profiler (VMP) (colored circles) transects across the outflow of the DIS. Transects are numbered from 1 to 4. Vectors depict the current velocity measured by shipboard Acoustic Doppler Current Profiler (ADCP) and are colored by conservative temperature (Θ, °C) measured by the VMP; both are averaged between 100 and 400 m. (c) Θ-S_A (Absolute salinity, g kg^{-1}) diagram colored by VMP transect (as in panel b) and CTDs (dark gray for outflow region and light gray for stations eastward of 113°W, as in panel a). Red contours indicate neutral density (γ^n, kg m^{-3}). Solid black lines are mixing lines between modified Circumpolar Deep Water (mCDW), Winter Water (WW) and glacial meltwater (MW, indicated by the arrow). In situ freezing temperature is shown by the dashed black line.

2.2. Turbulent Mixing Metrics

The rate of dissipation of turbulent kinetic energy (ε, W kg^{-1}) was calculated based on Oakey (1982). Following Naveira Garabato et al. (2017), shear variance was calculated approximately every 0.5 m (then, the profiles were 2-m bin-averaged), using shear spectra computed over 1-s bins integrated between 1 Hz and the spectral minimum in the 10–25 Hz band (or the 25 to 100-Hz band for $\varepsilon > 10^{-7}$ W kg^{-1}). Turbulent diapycnal diffusivity (κ, m^2 s^{-1}) was estimated based on Osborn (1980), with a mixing coefficient of 0.2, and N^2 calculated from the 10-m smoothed VMP profiles of temperature and salinity. Note that the bulk mixing coefficient can be even higher near the bottom for energetic overflows (e.g., Ijichi et al., 2020). Although we acknowledge this limitation in the Osborn model, we keep the value 0.2 to be consistent with other studies of mixing and turbulence in the vicinity of ice shelf outflows—for instance, Naveira Garabato et al. (2017).

Richardson number (Ri) was calculated as follows:

$$Ri = \frac{N^2}{\left(\frac{\partial u}{\partial z}\right)^2 + \left(\frac{\partial v}{\partial z}\right)^2} \quad (1)$$

where u and v are the horizontal components of velocity, and z is vertical distance.

We estimated the vertical heat (Q_h) and salt (Q_s) fluxes by:

$$Q_{tracer} = -\rho\kappa\left(\frac{\partial tracer}{\partial z}\right) \quad (2)$$

where ρ is in situ density and $\frac{\partial tracer}{\partial z}$ is the tracer vertical gradient. For Q_h, the specific heat capacity of seawater is also added to Equation 2.

2.3. Characterization of Instabilities

Ertel's potential vorticity (q, s^{-3}; Hoskins, 1974) was calculated by the approximation:

$$q \approx \left(f + \frac{\partial v_{as}}{\partial x}\right)N^2 - \left(\frac{\partial v_{as}}{\partial z}\right)\left(\frac{\partial b}{\partial x}\right) \quad (3)$$

where f is the local Coriolis parameter, v_{as} represents the along-slope velocity component obtained by rotating the zonal (u) and meridional (v) components 31° clockwise to follow the slope orientation (Figure 1b; positive velocity is north-northeast), $b = -g\frac{(\rho-\rho_0)}{\rho_0}$ is buoyancy (g is the acceleration due to gravity, and $\rho_0 = 1028\ kg\ m^{-3}$ is the reference density), and ∂x is the horizontal distance between stations. The choice for the along-slope rotation of the velocity does take the topography to be smoother than it actually is. However, the orientation of the velocity vectors in Figure 1b agrees with our smoothed topography. The data set was averaged into 16-m bins to match the vertical resolution of the SADCP observations prior calculating q.

A variety of instabilities might develop when q takes the opposite sign to f, which is negative in the Southern Hemisphere. This generates overturning instabilities termed gravitational, symmetric, and centrifugal, which extract kinetic energy from a combination of convective available potential energy, vertical and lateral shear production, respectively (Haine & Marshall, 1998). The criterion for instability is met when $\phi_{Ri_B} < \phi_C$, where $\phi_{Ri_B} = tan^{-1}\left(-Ri^{-1}\right)$ and the critical angle $\phi_C = tan^{-1}\left(-1 - f^{-1}\left(\frac{\partial v_{as}}{\partial x}\right)\right)$ (Thomas et al., 2013). When the criterion is met, the nature of the instability is determined from ϕ_{Ri_B}. Since $N^2 < 0$ was not observed in this data set, gravitational instability was not observed. Therefore, we evaluated the occurrence of symmetric instability, $-90° < \phi_{Ri_B} < -45°$ where $N^2 > 0$ and $\frac{\partial v_{as}}{\partial x}f^{-1} < 0$, or $-90° < \phi_{Ri_B} < \phi_C$ where $N^2 > 0$ and $\frac{\partial v_{as}}{\partial x}f^{-1} > 0$, and centrifugal instability, $\phi_{Ri_B} > -45°$ where $N^2 > 0$ and $\frac{\partial v_{as}}{\partial x}f^{-1} < 0$.

3. Results

3.1. Hydrographic Characterization of the Outflow at the Western DIS Front

A northeastward ocean current O (10 cm s^{-1}) flowing along-slope between the 300 and 500 m isobaths (Figure 1b) was observed at the western DIS front. Currents were weaker near the two ends of the transects or even reversed direction, for example, at the eastern end of transect 3. A core of relatively warm water (~0.1–0.2°C warmer than at the ends of the transects) was located approximately above the 500 m isobath (Figure 1b) (Although melting the ice cools and freshens the mCDW compared to the properties of mCDW as it enters the cavity, the resulting mixture is still warmer than the ambient water around the outflow region). This warm core contained glacially modified water exported from the DIS cavity, as is evident in Θ-S_A space: the observations collected within the core lie close to the mixing line between mCDW and meltwater (Gade, 1979). This is in contrast to the observations in the eastern DIS which lie toward the mCDW-Winter Water mixing line (Figure 1c).

Close to the ice front, there was a single deep core (>250 m) of northward flow (~15 cm/s; Transect 1; Figure 2a). Further from the ice, there was a second core, shallower than and to the west of the deep core (Transects 2, 3, and 4; Figures 2c–2e and 2g). Note that the greater apparent width of the shallower core at transect 2 arises because transect 2 is not perpendicular to the slope, unlike the other transects. The double-core structure of the outflow was also present in the ship-based CTD/LADCP measurements both near the ice shelf and further north (Figure S1 in Supporting Information S1).

Relatively high temperatures were observed between 150 and 250 m, toward the western end of the transects (Figures 2b– 2d, 2f and 2h and Figure S1 in Supporting Information S1) where the isopycnals (e.g., 27.45 and

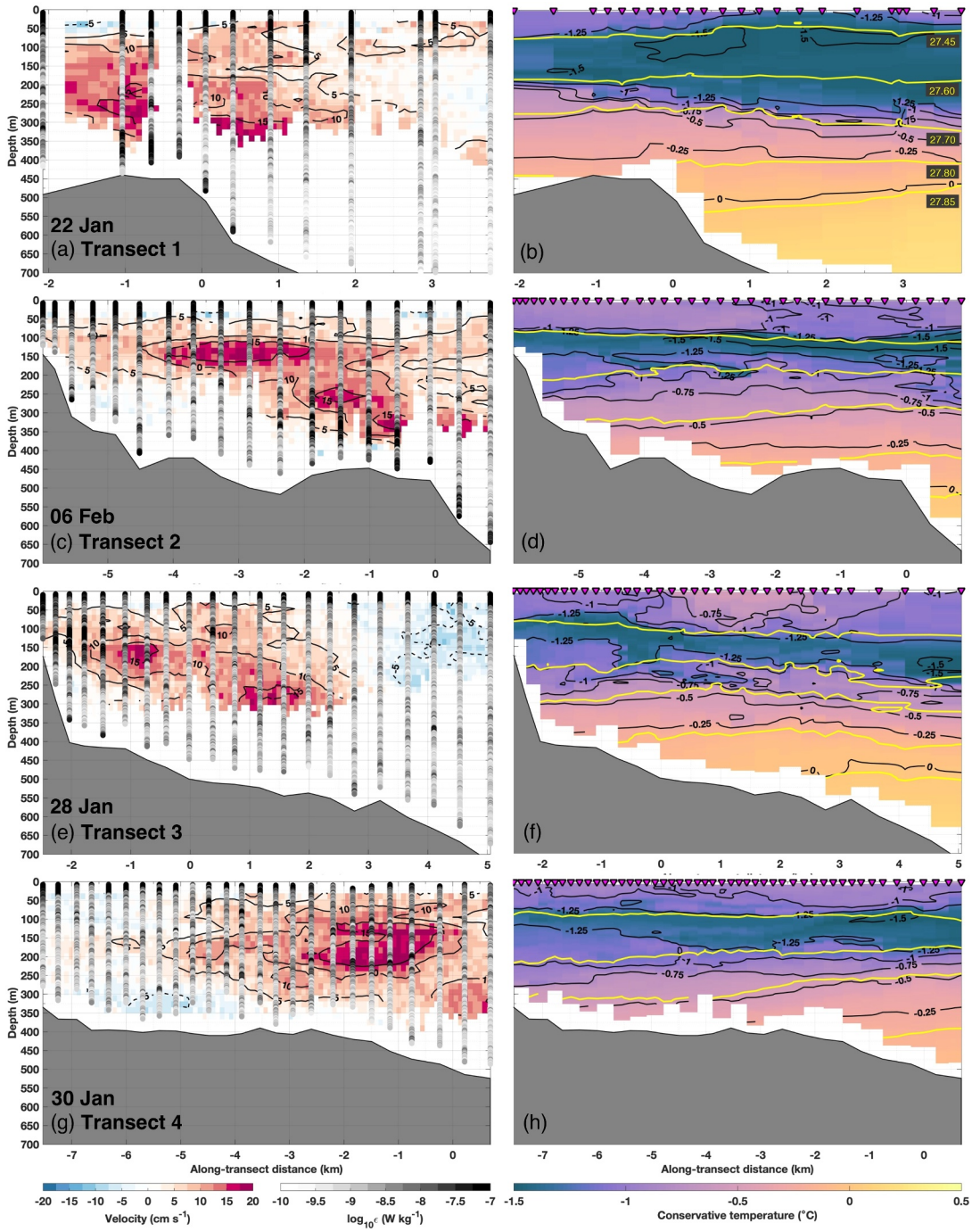

Figure 2. (a), (c), (e), and (g) Along-slope velocity (cm s^{-1}; positive velocity contours are indicated by solid lines, negative contours by dashed lines) and turbulent kinetic energy dissipation rate (ε, W kg^{-1}). Velocity is positive to the north-northeast. (b), (d), (f), and (h) Conservative temperature (°C). Isopycnals (neutral densities; γ^n) are plotted in yellow. In all panels, water depth recorded from the multibeam echo sounder at each VMP downcast is shown in gray; the *x*-axis shows the along-transect distance (km) from the 500 m isobath and differs between rows. (Note that turbulence is measured on downcast only; temperature and salinity are measured on down- and upcasts.)

27.60 kg m^{-3}) were generally further apart in the vertical, indicating low stratification. These observations are consistent with previous observations of glacially modified outflows in a strong, shallow current toward the western end of the DIS (e.g., Kim et al., 2021; Miles et al., 2016; Randall-Goodwin et al., 2015). The

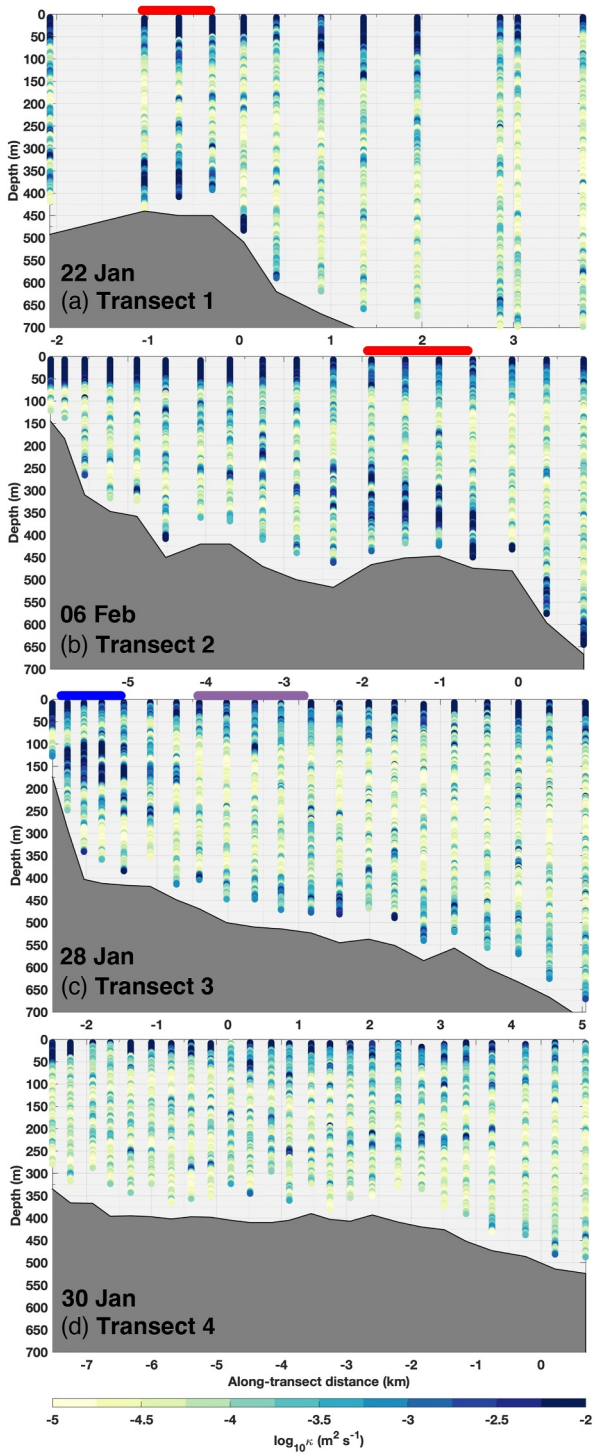

Figure 3. Turbulent diapycnal diffusivity (κ, $m^2\ s^{-1}$) for transects (a) 1, (b) 2, (c) 3, and (d) 4. Red, blue, and purple bars on panels (a), (b), and (c) mark the casts used to characterize the different turbulence patterns (see Figure 5). In all panels, water depth recorded from the multibeam echo sounder at each VMP downcast is shown in gray; the *x*-axis shows the along-transect distance (km) from the 500-m isobath and differs between rows.

measurements acquired from the VMP showed complex patches of relatively warm water interleaving cold water layers, mostly located in depths between 100 and 250 m (Figures 2d– 2f and 2h).

3.2. Turbulent Mixing Measurements at the Western DIS Front

There was large spatial variability in ε and κ in the DIS outflow (Figure 2), varying from O (10^{-9} W kg^{-1}) to O (10^{-7} W kg^{-1}) and O (10^{-4} $m^2\ s^{-1}$) to O (10^{-2} $m^2\ s^{-1}$), respectively (Figure 2). Areas of elevated turbulent mixing were relatively small and were highly localized in space. Below, we describe the main areas of elevated turbulent mixing for each transect.

In transects 1 and 2, elevated values of ε (O $\sim$ 10^{-7} W kg^{-1}) and κ O (10^{-2} $m^2\ s^{-1}$) were observed above a topographic rise from the seabed to depths of ∼100–200 m (Figures 2a, 2c, 3a and 3b). These were co-located with the strong northeastward currents of the deep outflow core. The two transects were occupied 15 days apart, suggesting that the bathymetric feature might be a consistent hotspot for generating turbulence near the seabed. Other sites of elevated turbulent mixing in these transects were associated with rough bathymetry both east and west of the topographic rise, in weakly stratified waters, and within regions of strong velocity (e.g., isotach > 15 cm s^{-1}).

In transect 3, elevated ε (∼10^{-7} W kg^{-1}) and κ O (10^{-2} $m^2\ s^{-1}$) were observed in a layer ∼100 m thick and ∼1 km wide at the western end (Figures 2e and 3c). This part of the transect was located between the core of the shallow current and the steep topography of the Dotson-Getz trough. The relatively warm waters near this area of turbulent mixing (see the shallowing of the −1.25°C isotherm) suggest a high concentration of glacial meltwater mixed with the mCDW (Figures 1c and 2f). Patches of relatively high temperature can be observed between interleaving layers of low temperature such as at the along-transect distance of 1–2 km east of the 500 m isobath (Figure 2f). Near the bottom, where stratification was reduced, κ showed slightly elevated values of O (10^{-3} $m^2\ s^{-1}$) (Figure 3c).

Transect 4, in the north and furthest from the ice front, showed elevated ε and κ surrounding the northward current core between 100 and 250 m west of the 500 m isobath (e.g., see isotach of 15 cm s^{-1}; Figures 2g and 3d). In the center of the core, where the velocity shear is weak, both ε and κ were reduced. As in transect 3, we observed relatively high temperature between interleaving layers of low temperature 2 km west of the 500 m isobath (Figure 2h), which was associated with the current core (Figure 2g).

3.3. Drivers of Turbulent Mixing at the DIS Front

In Section 3.2, we showed that turbulent mixing was localized over a topographic rise in transects 1 and 2, and with the outflow in shallow water in transect 3. We now explore possible causes of the elevated turbulent mixing with examples from transects 2 and 3. We chose these transects to exemplify the causes of turbulent mixing because they showed large areas of elevated ε and κ and the SADCP data have fewer gaps, which might be enough to provide indications of the drivers. Transect 4 showed a pattern of mixing that suggested shear-driven turbulence associated with the vertical shear of the shallow current (Figure 2g) and is not explored further. We exclude tidal-driven mixing because tidal velocities were relatively small, O (1 cm s^{-1}), in the region and all transects were surveyed in similar tidal conditions (Figure S2 in Supporting Information S1).

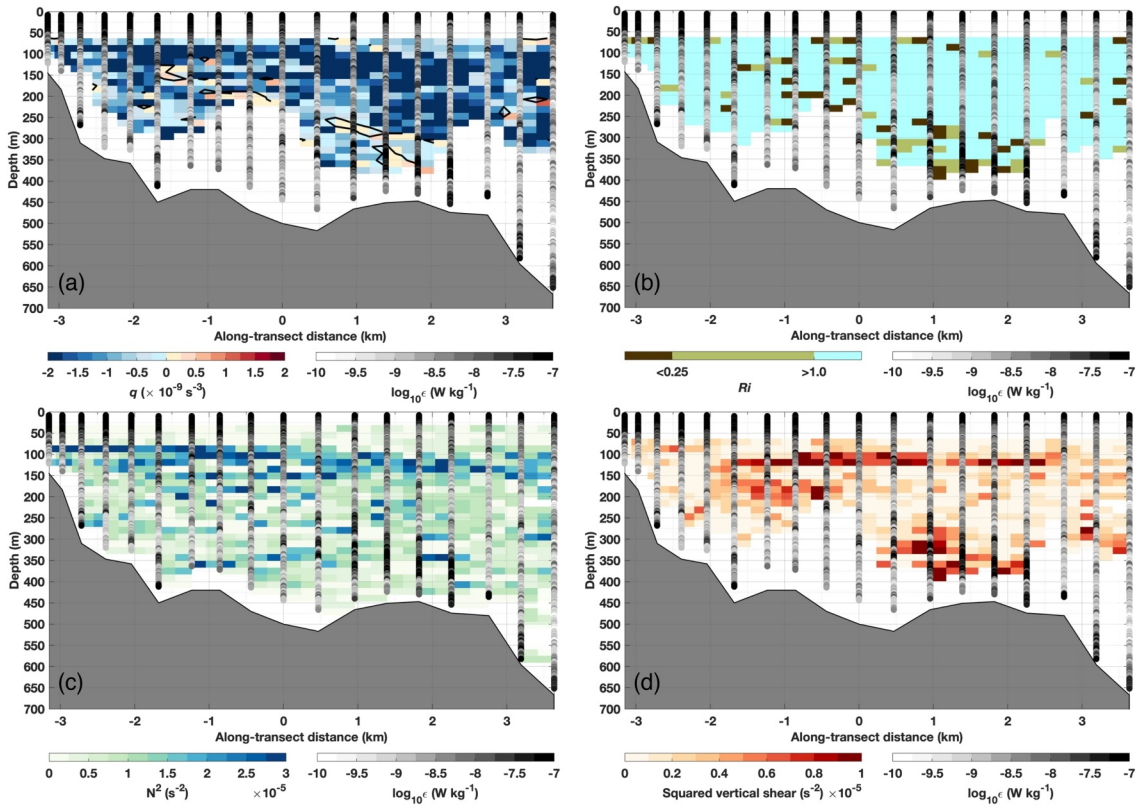

Figure 4. Turbulent mixing metrics for transect 2. (a) Ertel's potential vorticity (q, s^{-3}), with black contour line showing $q = 0\ s^{-3}$, (b) Richardson number (Ri), (c) Brunt-Väisälä frequency (N^2, s^{-2}), and (d) squared vertical shear (s^{-2}). Turbulent kinetic energy dissipation rate is plotted as in Figure 2 (ε, W kg^{-1}). In all panels, water depth recorded from the multibeam echo sounder at each VMP downcast is shown in gray; the x-axis shows the along-transect distance (km) from the 500-m isobath.

Overturning instability in stratified shear layers may develop when q takes the opposite sign to planetary vorticity (Hoskins, 1974), and when $Ri < 0.25$ (Hazel, 1972). Most of transect 2 is characterized by negative q and $Ri > 1$, indicating stable conditions. Small patches of positive q and $Ri < 0.25$ are observed near the topographic rise at the ~1 km along-transect distance between 250 and 300 m depth (Figures 4a and 4b). These areas are broadly co-located with low N^2 values and relatively high shear-squared values (Figures 4c and 4d). The lack of SADCP data below ~300 m preclude further analysis nearer the topographic rise. Given the deep current location (i.e., near a topographic rise) and its relatively high speeds (Figure 2c), the seabed could generate friction with the current, increasing vertical shear, or else the interaction with the seabed could trigger the breaking of internal waves, such as lee waves, which could generate turbulent mixing at large distances from the seabed (Sheen et al., 2013).

The western end of transect 3 is characterized by patches of low stratification and high vertical shear (Figures 5c and 5d). The area of elevated ε and κ is co-located with a larger region where positive q and $Ri < 0.25$ are present (Figures 5a and 5b). This indicates that vertical shear dominates over stratification, making the water column susceptible to shear-driven instabilities. N^2 was positive, which indicates that gravitational instability does not play a role in producing the turbulent pattern. In order to characterize the importance of Earth's rotation, we calculated the Rossby number, which is the ratio between the vertical component of relative vorticity and planetary vorticity, $Ro = \zeta/f \approx (\partial v_{as}/\partial x)/f$. Ro was large and negative ($Ro < -1$) in the western end of transect 3 (Figure 5e), indicating that ageostrophic effects become important. A large and negative Rossby number often corresponds to conditions where relative vorticity is strongly negative, making centrifugal instability more likely (Haine & Marshall, 1998). The instability classification shows that at the western end of transect 3, symmetric and centrifugal instabilities play a role in driving the overturnings, as evidenced by q and Ri conditions (Figures 5a, 5b and 5f).

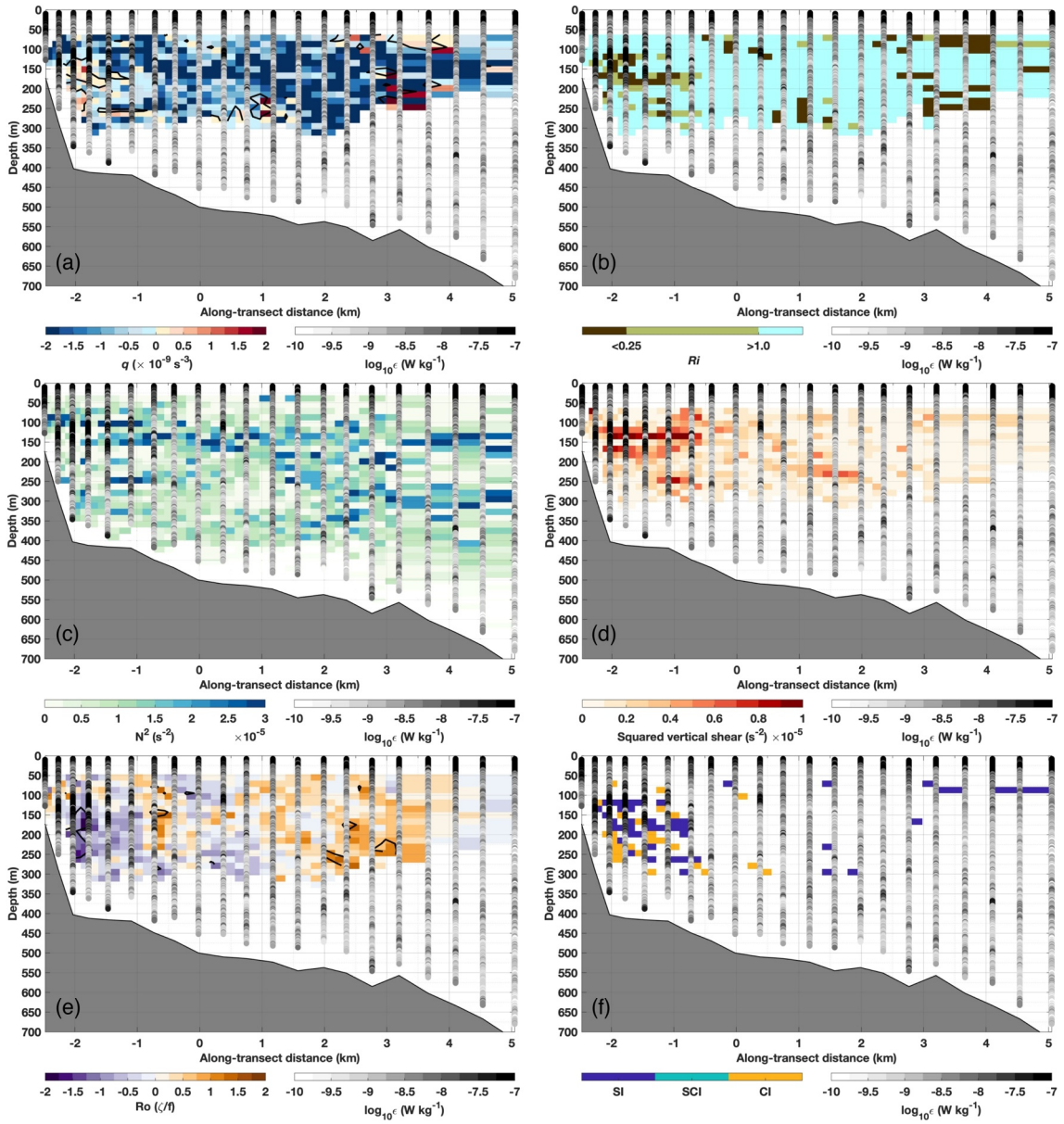

Figure 5. Turbulent mixing metrics for transect 3. (a) Ertel's potential vorticity (q, s^{-3}), with the black contour line $q = 0\ s^{-3}$, (b) Richardson number (Ri), (c) Brunt-Väisälä frequency (N^2, s^{-2}), (d) squared vertical shear (s^{-2}), (e) Rossby number (Ro), with black line showing $Ro = -1$, and (f) Instability classification (Thomas et al., 2013), where symmetric instability (SI), symmetric-centrifugal instability (SCI) and centrifugal instability (CI) are shown. Turbulent kinetic energy dissipation rate is plotted as in Figure 2 (ϵ, W kg^{-1}). In all panels, water depth recorded from the multibeam echo sounder at each VMP downcast is shown in gray; the x-axis shows the along-transect distance (km) from the 500 m isobath.

3.4. Vertical Heat and Salt Fluxes

The spatial pattern of turbulent mixing at the DIS front, and below the wind-driven upper layers, allowed us to group similar profiles into three patterns.

1. Pattern 1 represents high turbulent mixing near the seabed above a topographic rise
2. Pattern 2 represents the high turbulent mixing at shallow depths at the western end of transect 3
3. Pattern 3 represents regions of low mixing elsewhere.

To better quantify the importance of the local turbulent mixing observed in the DIS outflow, we calculated Q_h and Q_s using Equation 2 (Figure 6). Mean profiles of Q_h and Q_s were calculated, and the median values, presented

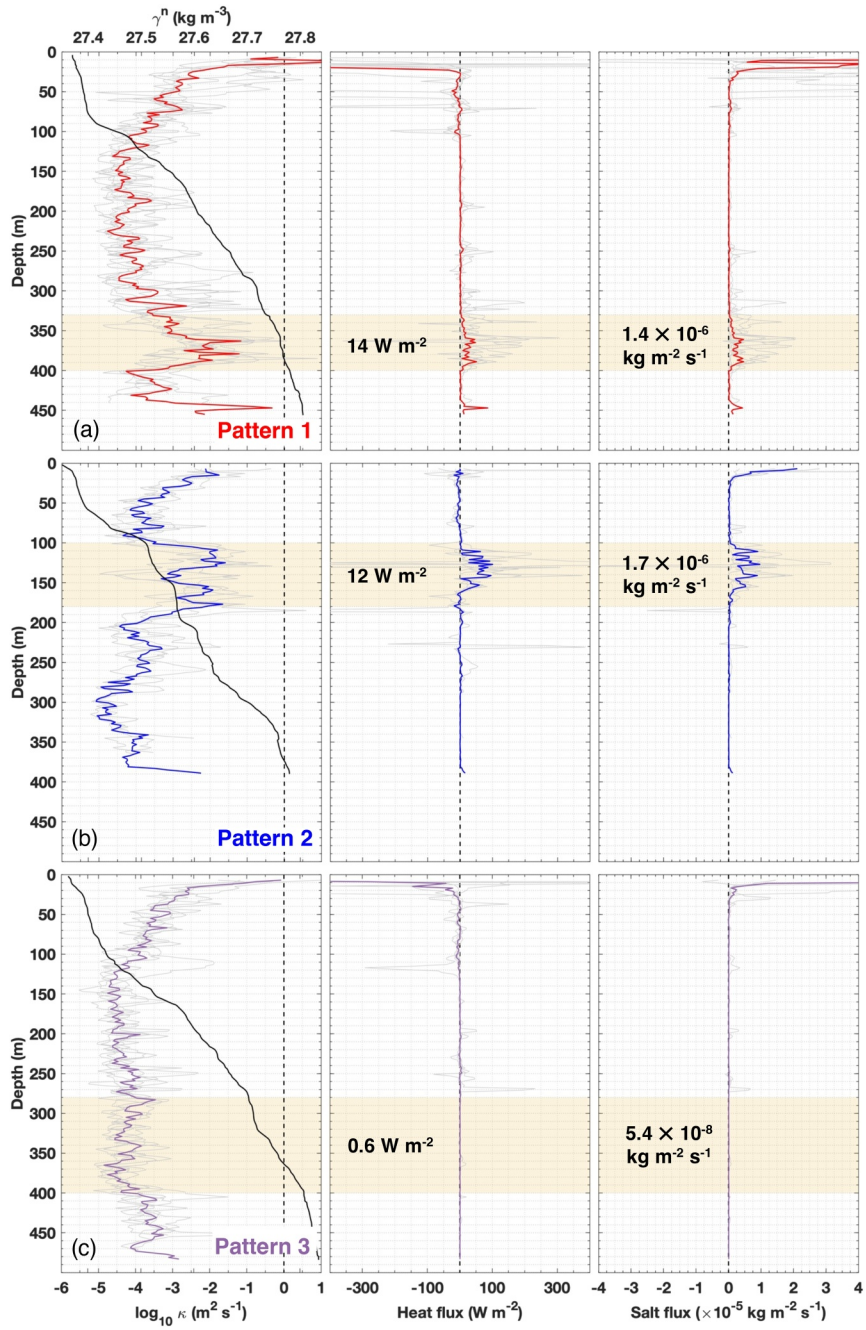

Figure 6. Characteristic turbulence patterns (left panels) and vertical heat (middle panels) and salt (right panels) fluxes. (Top row) Seven profiles (light gray) with high turbulent diapycnal diffusivity (κ), heat and salt fluxes near the seabed, were selected from transects 1 and 2 to represent pattern 1. Mean κ, heat and salt fluxes profiles are shown in red. (Middle row) As top row, but for pattern 2 using four selected profiles that correspond to high turbulence at middepth layers, as identified in transect 3 (Bottom row) As top row, but for low turbulence pattern 3 using five profiles selected from transect 3. Yellow shading depicts the depth range used to calculate the median heat and salt fluxes, shown by the bold numbers within the panels.

below, were calculated within depth ranges that characterized the elevated turbulent mixing in each pattern. For Pattern 1, we chose the depth range of 330–400 m, composed of mCDW (Figures 6a–6c). For Pattern 2, the depth range chosen was 100–180 m, which is composed of cold glacially meltwater-rich water (Figures 5d–5f). For Pattern 3, we chose an arbitrary depth range of 280–400 m that showed low turbulent mixing (Figures 6g–6i).

The median Q_h associated with Patterns 1 and 2 for the selected depth ranges were, respectively, 14 W m^{-2} and 12 W m^{-2}; for Q_s, the median values for the selected depth ranges were 1.4×10^{-6} kg m^{-2} s^{-1} and 1.7×10^{-6} kg m^{-2} s^{-1} respectively (Figures 6b, 6c, 6e and 6f). These are approximately two orders of magnitude above the values found in Pattern 3 (0.6 W m^{-2} and 5.4×10^{-8} kg m^{-2} s^{-1}, respectively; Figure 5c). If the turbulence, and consequently the vertical fluxes, in Patterns 1 and 2 were constant in time, integrating Q_h and Q_s over a year would lead to an increase in temperature and salinity of the overlying upper layers in the order of 1°C and ∼0.6 g kg^{-1}, respectively.

Taking Pattern 2 (transect 3) as an example, we can estimate the approximate offshore distance where enhanced mixing is acting to dilute the heat associated with the outflow. Using the equation below, and taking averaged values between 100 and 180 m depth, where mixing is strongest:

$$Horizontal\ lengthscale\ of\ dilution = velocity \times \left(\frac{\Delta T^2}{\kappa \times \left(\frac{\partial T}{\partial z} \right)^2} \right) \quad (4)$$

where ΔT is the temperature anomaly (relative to the surrounding waters) and $\frac{\partial T}{\partial z}$ is the vertical gradient of temperature, we find a horizontal lengthscale for dilution of thermal energy of 325 km. Note that this back-of-the-envelope calculation does not consider the temporal and spatial variability associated with variability of mixing and velocity, nor other sources of mixing, such as baroclinic instabilities, that could increase the dissipation of heat. Nonetheless, the lengthscale found here broadly agrees with glacial meltwater distribution identified through noble gases (Biddle et al., 2019; Kim et al., 2016).

4. Discussion

The high spatial resolution (the average distance between casts was ∼420 m) of the VMP and SADCP measurements allowed us to characterize in unprecedented detail the outflow system in front of the DIS. Previous surveys have shown the existence of the high meltwater content associated with the outflow current (e.g., Kim et al., 2021; Miles et al., 2016; Randall-Goodwin et al., 2015; Yang et al., 2022), but their low spatial resolution did not capture the different branches of the outflow current in details. Here, we report a current system formed of two main cores, on either side of the 500 m isobath. The warmer deeper core lies closer to the mCDW layers (Figure 2) and it is mixed with glacial meltwater (Figure 1c). The shallow core might be associated with buoyant flows leaving the DIS cavity guided by the basal channels that connect the inner ice shelf to the calving front (Wåhlin et al., 2024). Our results are consistent with the fast currents in the western side of the DIS revealed by an autonomous underwater vehicle (Wåhlin et al., 2024). These authors showed a smoother and more eroded ice base in the western side than its eastern side, which is driven by the fast currents beneath the ice base producing strong shear that allows large vertical heat fluxes nearer the ice base. A large portion of the DIS basal melting occurs within the basal channels (Gourmelen et al., 2017). The intensity of the outflow currents is modulated by the seasonal (Yang et al., 2022) and interannual (Kim et al., 2021) variability associated with the inflow of mCDW through the Dotson-Getz trough and by the baroclinic component that enters the ice shelf cavity (Wåhlin et al., 2020). Both regulate the amount of heat entering the cavity which induces basal melting and consequently changes the vertical density structure of the outflow region.

At the DIS front, the elevated turbulent mixing is mainly shear-driven and induced by the interaction of the fast (O (15) cm s^{-1}) ocean currents leaving its cavity with the rough topography (Figures 4 and 5). Two high-mixing patterns were observed: one near the seabed associated with a topographic rise (Pattern 1); and another at shallow depths at the western side of the Dotson-Getz Trough (Pattern 2). In Pattern 1, the near-bed turbulent mixing in front of the DIS front is at least an order of magnitude higher than near-bed mixing observed thus far elsewhere in West Antarctica's shelf seas—for instance, over a topographic ridge (Scott et al., 2021) and over the seabed within the PIIS cavity (Kimura et al., 2016). In these two regions, the low current speeds are not sufficient to overcome the weak stratification to induce turbulent mixing as high as observed at the DIS. At the DIS, we hypothesize that the breaking of internal waves, such as lee waves, at the topographic rise might play a role in promoting the high observed mixing rates observed there. In Pattern 2, the dominant forms of instabilities (transect 4) were symmetric, that is, driven by vertical shear production, and centrifugal, that is, driven by lateral shear production (Figure 5f); both mechanisms can produce kinetic energy for turbulent mixing (Thomas et al., 2013). This

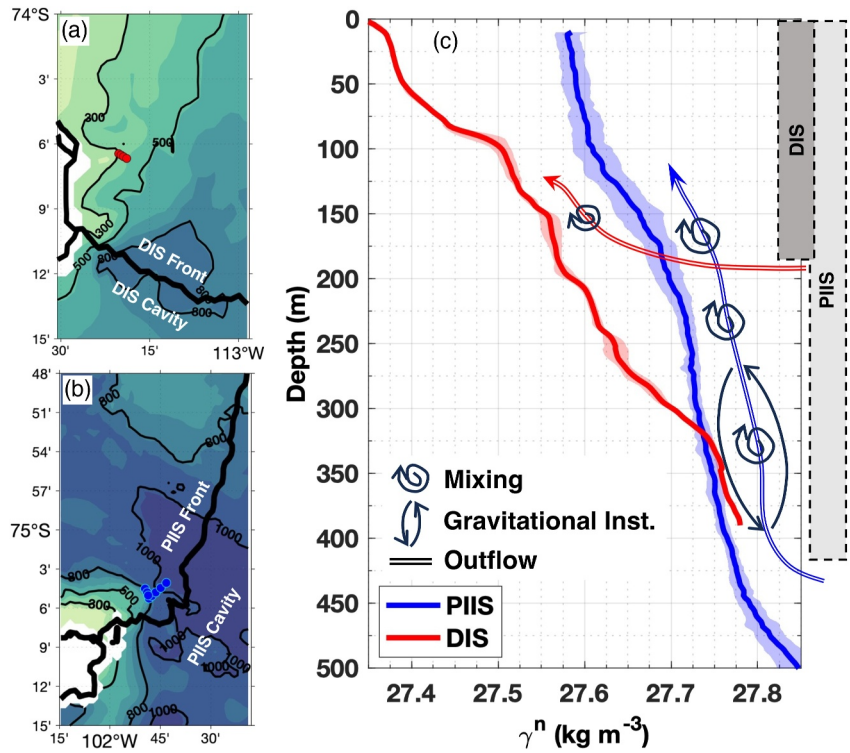

Figure 7. (a) Downcast CTD stations 2–5 from transect 3 at the western DIS front. (b) Downcast stations at the western PIIS front were collected in February 2014 (Naveira Garabato et al., 2017). Bathymetry and colormap follow Figure 1b. (c) Averaged neutral density (γ^n) for the DIS (red) and the PIIS (blue) profiles taken from panels (a) and (b), respectively. The shadings show ±1 standard deviation from the mean. The DIS and the PIIS ice drafts are depicted in gray and were based on Wåhlin et al. (2024) and Naveira Garabato et al. (2017), respectively.

combination of instabilities resulted in a positive q (Figure 5a) and low Ri (Figure 5b), both of which are favorable for mixing. The homogenization of the water column, derived from the turbulent mixing in Pattern 2, could lead subsequently to stronger turbulent mixing given the resulting lowered stratification (Figure 5d). At the DIS front, mCDW is a reservoir of heat available below the thermocline and turbulent mixing significantly enhances vertical heat and salt fluxes to the thermocline and upper layers (Figures 5b, 5c, 5e and 5f). Topography-induced and strong vertical shear might be common features of many ice shelf outflows, which strengthens the general applicability of our results. Moreover, limited knowledge of the bathymetry in the vicinity of ice shelf fronts leads to poor bathymetry maps that are later fed into numerical models. Given these limitations and the fact that the bathymetric rise at the DIS front is of similar magnitude as the vertical resolution of typical numerical models (~50 m, Figure 2c), the topography-induced mixing might not be accurately represented in simulations.

The magnitudes of ε and κ we observed at the DIS were similar to those reported by Naveira Garabato et al. (2017) in the upper layers of the outflow from beneath Pine Island Ice Shelf (PIIS). Further, the complex patchiness of warm water interleaving with cold water layers between 100 and 250 m resembles the PIIS front, where a buoyant meltwater plume leaves the cavity at the depth of the thermocline during summer (Zheng et al., 2021). At the PIIS, the ascending meltwater generates strong mixing by gravitational instability, and by centrifugal instability that grows by extracting kinetic energy from the lateral shear. Both instabilities lead to strong turbulent mixing ($O \sim 10^{-7}$ W kg^{-1}; Naveira Garabato et al., 2017). Although in Pattern 2, we observed overturning instability, as indicated by positive q (Figure 5a) and low Ri (Figure 5b), there was no gravitational instability (Figure 5f). A possibility for this difference might be the shallow draft of the DIS (~180 m; Wåhlin et al., 2024): waters exiting the cavity are injected close to the depth of neutral buoyancy and so do not produce the vigorous mixing through gravitational instability as they ascend (Figure 7). Conversely, the deep draft of the PIIS (~400 m; Figure 6; Naveira Garabato et al., 2017) is such that outflowing buoyant water is injected into dense ambient waters and needs to ascend (Arnscheidt et al., 2021).

Our observations of elevated mixing in the DIS outflow, together with those from other glacial outflows and from across the continental shelf of West Antarctica, suggest that ice shelf outflows are hotspots of high turbulent mixing that play an outsized role in water mass transformation over the shelf. The turbulent mixing in Patterns 1 and 2 was an order of magnitude greater than that observed elsewhere on the shelf (Kimura et al., 2016; Scott et al., 2021); and the attendant turbulent fluxes of heat and salt are two orders of magnitude greater than those in more quiescent regions (i.e., Pattern 3). Given: (a) the low stratification common to the polar oceans; and (b) the strong currents common to the outflows from beneath fast-melting ice shelves (Grosfeld et al., 1997), susceptible as they are to symmetric and centrifugal instabilities, we hypothesize that strong turbulent mixing is a feature of ice shelf outflow currents. The elevated vertical fluxes associated with this mixing mean that outflow currents have the potential to exert a strong control on the distribution of heat, salt and trace elements—for instance, iron and nutrients—in polar waters. The intensified mixing might help dissolved trace elements to be entrained into the Winter Water layer, and in the coming winter, when the mixed layer deepens, be entrained near the surface to boost the phytoplankton bloom in the following spring. Our estimate suggests that the dilution of heat, and potentially other tracers, can be propagated over hundreds of kilometers away from the ice shelf front, which agrees with tracers from observations (Biddle et al., 2019; Kim et al., 2016) and also simulated by ocean models (e.g., Kimura et al., 2017; Nakayama et al., 2020).

Models usually fail to resolve submesoscale turbulence properly. Turbulent mixing parameterizations should consider the peculiarities of local ocean conditions (e.g., ice shelf fronts) to reduce the inaccuracy of mixing rates associated with empirical closure constants. Our findings suggest that the dissipation rates should be tuned to higher values near ice shelf fronts, specifically where seabed topography has complex features and where glacial meltwater is injected in subsurface depths (Swart et al., 2023). We showed that high dissipation was associated with strong vertical shear of outflow currents leaving the ice shelf cavities, which seems to be a common feature in large melting ice shelves (e.g., Figure 2 and Naveira Garabato et al., 2017). To overcome computationally costly hybrid approach with large eddy simulation for high shear regions, models could be combined with machine learning techniques (Feng et al., 2024) that identify the patterns of turbulence (Couchman et al., 2021), as well as having good bathymetric observations in front of ice shelves.

Different timescales have been reported to influence the variability of the ocean in the Amundsen Sea, including seasonal (Yang et al., 2022), interannual (Dutrieux et al., 2014; Kim et al., 2021) and even decadal (Jenkins et al., 2018). All these sorts of variability might play a role in changing the outflow intensity and the vertical stratification field in front of the DIS. Moreover, ice shelf melting is expected to increase with the West Antarctica ocean warming by the end of the century (Naughten et al., 2023). The increase in the ice shelf melting would likely lead to stronger outflow, and therefore more mixing. With the enhanced mixing at the subsurface, it is plausible to hypothesize that more heat could reach the sea surface, and therefore facilitate the sea ice melting and reduction near the ice shelf and potentially increase the risks for ice shelf instability through calving (Massom et al., 2018).

5. Conclusions

Here we identified two main patterns of elevated ε and κ in the DIS outflow: (a) near the bottom above a topographic rise at the transects closer to the DIS front, and (b) at middepth layers in areas further north. The two high-mixing patterns exhibit large shear associated with the strong outflow currents leaving the DIS cavity. Vertical fluxes of heat and salt in these two patterns were on the order of O (10) W m and O ($1e10^{-6}$) kg m^2 s^{-1}. At least in the deeper turbulent pattern, the mixing seems to be a consistent feature over time. The highly localized nature of mixing processes presents a challenge for ocean and climate models, as accurately capturing these dynamics requires realistic bathymetry and advanced small-scale parameterizations. Because of the scarcity of fine-scale observations in front of ice shelves, our data set is particularly valuable—not only in improving the limited understanding of turbulence in front of complex, fast-melting ice shelves but also in providing crucial validation for ocean models.

Data Availability Statement

BedMachine Antarctic v3 is available in Morlighem (2022). CATS2008 is available at https://www.esr.org/research/polar-tide-models/list-of-polar-tide-models/cats2008/. The CTD data set is available in NSF/NERC

ARTEMIS and ITGC TARSAN (2024). SADCP data set is available in Wellner (2022). VMP data set is available in Dotto et al. (2024). TEOS-10 and Pre-TEOS10 software are available at https://www.teos-10.org/index.htm.

Acknowledgments
We thank the scientists, technicians, and ship crew involved in the ocean data collection during the cruise NBP22-02. Logistics were provided by NSF-U.S. Antarctic Program and NERC-British Antarctic Survey. This work is from the Thwaites-Amundsen Regional Survey and Network Integrating Atmosphere-Ice-Ocean Processes (TARSAN) project, a component of the International Thwaites Glacier Collaboration (ITGC; https://thwaitesglacier.org/). TSD, KJH, and RAH were supported by TARSAN project Grant NE/S006419/1. TSD was supported by U. K. Natural Environment Research Council National Capability Program AtlantiS (NE/Y005589/1). KJH, RAH, and YZ were supported by ARTEMIS project (NE/W007045/1). KJH, PMFS and YZ were supported by the COMPASS project (Grant 741120), which was funded by the European Research Council under the Horizon 2020 program. GMD was supported by the COMPASS project and the European Union's Horizon 2020 Research and Innovation Program under the Marie Skłodowska-Curie grant agreement No 101034309. We thank A. C. Naveira Garabato, A. Forryan, and C. Spingys for their support and guidance in processing the VMP data. We thank A. C. Naveira Garabato for discussions on the instability processes. We thank Julia Hummon for re-processing the SADCP data. This is ITGC Contribution No. ITGC-110.

References

Arnscheidt, C. W., Marshall, J., Dutrieux, P., Rye, C. D., & Ramadhan, A. (2021). On the settling depth of meltwater escaping from beneath Antarctic ice shelves. *Journal of Physical Oceanography*. https://doi.org/10.1175/JPO-D-20-0286.1

Biddle, L. C., Loose, B., & Heywood, K. J. (2019). Upper ocean distribution of glacial meltwater in the Amundsen Sea, Antarctica. *Journal of Geophysical Research: Oceans*, *124*(10), 6854–6870. https://doi.org/10.1029/2019JC015133

Couchman, M. M. P., Wynne-Cattanach, B., Alford, M. H., Caulfield, C.-c. P., Kerswell, R. R., MacKinnon, J. A., & Voet, G. (2021). Data-driven identification of turbulent oceanic mixing from observational microstructure data. *Geophysical Research Letters*, *48*(23), e2021GL094978. https://doi.org/10.1029/2021GL094978

de Lavergne, C., Madec, G., Le Sommer, J., Nurser, A. J. G., & Naveira Garabato, A. C. (2016). On the consumption of Antarctic bottom water in the Abyssal ocean. *Journal of Physical Oceanography*, *46*(2), 635–661. https://doi.org/10.1175/JPO-D-14-0201.1

Depoorter, M., Bamber, J., Griggs, J., Lenaerts, J. T. M., Ligtenberg, S. R. M., van den Broeke, M. R., & Moholdt, G. (2013). Calving fluxes and basal melt rates of Antarctic ice shelves. *Nature*, *502*(7469), 89–92. https://doi.org/10.1038/nature12567

Dinniman, M. S., St-Laurent, P., Arrigo, K. R., Hofmann, E. E., & Van Dijken, G. L. (2020). Analysis of iron sources in Antarctic continental shelf waters. *Journal of Geophysical Research: Oceans*, *125*(5). https://doi.org/10.1029/2019JC015736

Dotto, T. S., Heywood, K., & Rob, A. H. (2024). VMP and SADCP at Dotson ice shelf outflow (2022). *Zenodo*. [Dataset]. https://doi.org/10.5281/zenodo.14008304

Dutrieux, P., De Rydt, J., Jenkins, A., Holland, P. R., Ha, H. K., Lee, S. H., et al. (2014). Strong sensitivity of Pine Island ice-shelf melting to climatic variability. *Science*, *343*(6167), 174–178. https://doi.org/10.1126/science.1244341

Feng, Q., Han, G., Liu, Y., Lin, X., Li, B., Gao, X., et al. (2024). Application of data-driven mixing parameterization scheme in a regional ocean model. *Ocean Modelling*, *188*, 102325. https://doi.org/10.1016/j.ocemod.2024.102325

Gade, H. G. (1979). Melting of ice in sea water: A primitive model with application to the Antarctic Ice Shelf and Icebergs. *Journal of Physical Oceanography*, *9*(1), 189–198. https://doi.org/10.1175/1520-0485(1979)009<0189:MOIISW>2.0.CO;2

Gourmelen, N., Goldberg, D. N., Snow, K., Henley, S. F., Bingham, R. G., Kimura, S., et al. (2017). Channelized melting drives thinning under a Rapidly melting Antarctic ice shelf. *Geophysical Research Letters*, *44*(19), 9796–9804. https://doi.org/10.1002/2017GL074929

Greene, C. A., Gardner, A. S., Schlegel, N.-J., & Fraser, A. D. (2022). Antarctic calving loss rivals ice-shelf thinning. *Nature*, *609*(7929), 948–953. https://doi.org/10.1038/s41586-022-05037-w

Grosfeld, K., Gerdes, R., & Determann, J. (1997). Thermohaline circulation and interaction between ice shelf cavities and the adjacent open ocean. *Journal of Geophysical Research*, *102*(C7), 15595–15610. https://doi.org/10.1029/97JC00891

Haine, T. W., & Marshall, J. (1998). Gravitational, symmetric, and baroclinic instability of the ocean mixed layer. *Journal of Physical Oceanography*, *28*, 634–658. https://doi.org/10.1175/1520-0485(1998)028,0634:GSABIO.2.0.CO;2

Hazel, P. (1972). Numerical studies of the stability of inviscid stratified shear flows. *Journal of Fluid Mechanics*, *51*(1), 39–61. https://doi.org/10.1017/S0022112072001065

Hoskins, B. J. (1974). The role of potential vorticity in symmetric stability and instability. *Quarterly Journal of the Royal Meteorological Society*, *100*(425), 480–482. https://doi.org/10.1002/qj.49710042520

Hummon, J., & Firing, E. (2003). A direct comparison of two RDI shipboard ADCPs: A 75-kHz ocean surveyor and a 150-kHz Narrowband. *Journal of Atmospheric and Oceanic Technology*, *20*(6), 872–888. https://doi.org/10.1175/1520-0426(2003)020<0872:ADCOTR>2.0.CO;2

Ijichi, T., St. Laurent, L., Polzin, K. L., & Toole, J. M. (2020). How variable is mixing efficiency in the abyss? *Geophysical Research Letters*, *47*(7), e2019GL086813. https://doi.org/10.1029/2019GL086813

Jackett, D. R., & McDougall, T. J. (1997). A neutral density variable for the World's oceans. *Journal of Physical Oceanography*, *27*(2), 237–263. https://doi.org/10.1175/1520-0485(1997)027<0237:ANDVFT>2.0.CO;2

Jenkins, A., Shoosmith, D., Dutrieux, P., Jacobs, S., Kim, T. W., Lee, S. H., et al. (2018). West Antarctic ice sheet retreat in the Amundsen Sea driven by decadal oceanic variability. *Nature Geoscience*, *11*(10), 733–738. https://doi.org/10.1038/s41561-018-0207-4

Jourdain, N. C., Mathiot, P., Merino, N., Durand, G., Le Sommer, J., Spence, P., et al. (2017). Ocean circulation and sea-ice thinning induced by melting ice shelves in the Amundsen Sea. *Journal of Geophysical Research: Oceans*, *122*(3), 2550–2573. https://doi.org/10.1002/2016JC012509

Kim, I., Hahm, D., Rhee, T. S., Kim, T. W., Kim, C.-S., & Lee, S. H. (2016). The distribution of glacial meltwater in the Amundsen Sea, Antarctica, revealed by dissolved helium and neon. *Journal of Geophysical Research: Oceans*, *121*(3), 1654–1666. https://doi.org/10.1002/2015JC011211

Kim, T., Yang, H. W., Dutrieux, P., Wåhlin, A. K., Jenkins, A., Kim, Y. G., et al. (2021). Interannual variation of modified circumpolar deep water in the Dotson-Getz Trough, west Antarctica. *Journal of Geophysical Research: Oceans*, *126*(12). https://doi.org/10.1029/2021JC017491

Kimura, S., Jenkins, A., Dutrieux, P., Forryan, A., Naveira Garabato, A. C., & Firing, Y. (2016). Ocean mixing beneath pine Island glacier ice shelf, west Antarctica. *Journal of Geophysical Research: Oceans*, *121*(12), 8496–8510. https://doi.org/10.1002/2016JC012149

Kimura, S., Jenkins, A., Regan, H., Holland, P. R., Assmann, K. M., Whitt, D. B., et al. (2017). Oceanographic controls on the variability of ice-shelf basal melting and circulation of glacial meltwater in the Amundsen Sea Embayment, Antarctica. *Journal of Geophysical Research: Oceans*, *122*(12), 10131–10155. https://doi.org/10.1002/2017JC012926

Massom, R. A., Scambos, T. A., Bennetts, L. G., Reid, R., Squire, V. A., & Stammerjohn, S. E. (2018). Antarctic ice shelf disintegration triggered by sea ice loss and ocean swell. *Nature*, *558*(7710), 383–389. https://doi.org/10.1038/s41586-018-0212-1

McDougall, T. J., & Barker, P. M. (2011). *Getting started with TEOS-10 and the gibbs seawater (GSW) oceanographic toolbox*. SCOR/IAPSO WG127.

Miles, T., Lee, S. H., Wåhlin, A., Ha, H. K., Kim, T. W., Assmann, K. M., & Schofield, O. (2016). Glider observations of the Dotson ice shelf outflow. *Deep Sea Research Part II: Topical Studies in Oceanography*, *123*, 16–29. https://doi.org/10.1016/j.dsr2.2015.08.008

Milillo, P., Rignot, E., Rizzoli, P., Scheuchl, B., Mouginot, J., Bueso-Bello, J. L., et al. (2022). Rapid glacier retreat rates observed in West Antarctica. *Nature Geoscience*, *15*(1), 48–53. https://doi.org/10.1038/s41561-021-00877-z

Morlighem, M. (2022). MEaSUREs BedMachine Antarctica, version 3. *Boulder, Colorado USA. NASA National Snow and Ice Data Center Distributed Active Archive Center*. [Dataset]. https://doi.org/10.5067/FPSU0V1MWUB6

Morlighem, M., Rignot, E., Binder, T., Blankenship, D., Drews, R., Eagles, G., et al. (2020). Deep glacial troughs and stabilizing ridges unveiled beneath the margins of the Antarctic ice sheet. *Nature Geoscience*, *13*(2), 132–137. https://doi.org/10.1038/s41561-019-0510-8

Nakayama, Y., Timmermann, R., & H. Hellmer, H. (2020). Impact of West Antarctic ice shelf melting on southern ocean hydrography. *The Cryosphere*, *14*(7), 2205–2216. https://doi.org/10.5194/tc-14-2205-2020

Naughten, K. A., Holland, P. R., & De Rydt, J. (2023). Unavoidable future increase in West Antarctic ice-shelf melting over the twenty-first century. *Nature Climate Change*, *13*(11), 1222–1228. https://doi.org/10.1038/s41558-023-01818-x

Naveira Garabato, A. C., Forryan, A., Dutrieux, P., Brannigan, L., Biddle, L. C., Heywood, K. J., et al. (2017). Vigorous lateral export of the meltwater outflow from beneath an Antarctic ice shelf. *Nature*, *542*(7640), 219–222. https://doi.org/10.1038/nature208251

NSF/NERC ARTEMIS and ITGC TARSAN. (2024). Vertical ocean profiles collected by a Conductivity-Temperature-Depth (CTD) package in the Amundsen Sea. *U.S. Antarctic Program (USAP) Data Center*. [Dataset]. https://doi.org/10.15784/601785

Oakey, N. S. (1982). Determination of the rate of dissipation of turbulent energy from simultaneous temperature and velocity shear microstructure measurements. *Journal of Physical Oceanography*, *12*(3), 256–271. https://doi.org/10.1175/1520-0485(1982)012<0256:DOTROD>2.0.CO;2

Osborn, T. R. (1980). Estimates of the local rate of vertical diffusion from dissipation measurements. *Journal of Physical Oceanography*, *10*(1), 83–89. https://doi.org/10.1175/1520-0485(1980)010<0083:EOTLRO>2.0.CO;2

Padman, L., Fricker, H. A., Coleman, R., Howard, S., & Erofeeva, L. (2002). A new tide model for the Antarctic ice shelves and seas. *Annals of Glaciology*, *34*, 247–254. https://doi.org/10.3189/172756402781817752

Polzin, K. L., Toole, J. M., Ledwell, J. R., & Scmitt, R. W. (1997). Spatial variability of turbulent mixing in the Abyssal ocean. *Science*, *276*(5309), 93–96. https://doi.org/10.1126/science.276.5309.93

Randall-Goodwin, E., Meredith, M. P., Jenkins, A., Yager, P. L., Sherrell, R. M., Abrahamsen, E. P., et al. (2015). Freshwater distributions and water mass structure in the Amundsen Sea Polynya region, Antarctica. *Elementa: Science of the Anthropocene*, *3*, 000065. https://doi.org/10.12952/journal.elementa.000065

Rignot, E., Mouginot, J., Scheuchl, B., van den Broeke, M., van Wessem, M. J., & Morlighem, M. (2019). Four decades of Antarctic ice sheet mass balance from 1979–2017. *Proceedings of the National Academy of Sciences*, *116*(4), 1095–1103. https://doi.org/10.1073/pnas.1812883116

Scott, R. M., Brearley, J. A., Naveira Garabato, A. C., Venables, H. J., & Meredith, M. P. (2021). Rates and mechanisms of turbulent mixing in a coastal embayment of the West Antarctic Peninsula. *Journal of Geophysical Research: Oceans*, *126*(5). https://doi.org/10.1029/2020JC016861

Sheen, K. L., Brearley, J. A., Naveira Garabato, A. C., Smeed, D. A., Waterman, S., Ledwell, J. R., et al. (2013). Rates and mechanisms of turbulent dissipation and mixing in the Southern ocean: Results from the diapycnal and isopycnal mixing experiment in the southern ocean (DIMES). *Journal of Geophysical Research: Oceans*, *118*(6), 2774–2792. https://doi.org/10.1002/jgrc.20217

Sherrell, R. M., Lagerström, M. E., Forsch, K. O., Stammerjohn, S. E., & Yager, P. L. (2015). Dynamics of dissolved iron and other bioactive trace metals (Mn, Ni, Cu, Zn) in the Amundsen Sea Polynya, Antarctica. *Elementa: Science of the Anthropocene*, *3*, 000071. https://doi.org/10.12952/journal.elementa.000071

Silvano, A., Rintoul, S. R., Peña-Molino, B., Hobbs, W. R., van Wijk, E., Aoki, S., et al. (2018). Freshening by glacial meltwater enhances melting of ice shelves and reduces formation of Antarctic Bottom Water. *Science Advances*, *4*(4), eaap9467. https://doi.org/10.1126/sciadv.aap9467

Swart, N. C., Martin, T., Beadling, R., Chen, J.-J., Danek, C., England, M. H., et al. (2023). The Southern Ocean Freshwater Input from Antarctica (SOFIA) initiative: Scientific objectives and experimental design. *Geoscientific Model Development*, *16*(24), 7289–7309. https://doi.org/10.5194/gmd-16-7289-2023

Thomas, L. N., Taylor, J. R., Ferrari, R., & Joyce, T. M. (2013). Symmetric instability in the Gulf Stream. *Deep Sea Research Part II: Topical Studies in Oceanography*, *91*, 96–110. https://doi.org/10.1016/j.dsr2.2013.02.025

Thompson, A. F., Speer, K. G., & Schulze Chretien, L. M. (2020). Genesis of the Antarctic slope current in West Antarctica. *Geophysical Research Letters*, *47*(16), e2020GL087802. https://doi.org/10.1029/2020GL087802

Thurnherr, A. M. (2021). How to process LADCP data with the LDEO. *Software*. Retrieved from https://www.ldeo.columbia.edu/~ant/LADCP.html

van Manen, M., Aoki, S., Brussaard, C. P. D., Conway, T. M., Eich, C., Gerringa, L. J. A., et al. (2022). The role of the Dotson ice shelf and circumpolar deep water as driver and source of dissolved and particulate iron and manganese in the Amundsen Sea polynya, southern ocean. *Marine Chemistry*, *246*, 104161. https://doi.org/10.1016/j.marchem.2022.104161

Wåhlin, A., Alley, K. E., Begeman, C., Hegrenæs, Ø., Yuan, X., Graham, A. G. C., et al. (2024). Swirls and scoops: Ice base melt revealed by multibeam imagery of an Antarctic ice shelf. *Science Advances*, *10*(31), eadn9188. https://doi.org/10.1126/sciadv.adn9188

Wåhlin, A. K., Steiger, N., Darelius, E., Assmann, K. M., Glessmer, M. S., Ha, H. K., et al. (2020). Ice front blocking of ocean heat transport to an Antarctic ice shelf. *Nature*, *578*(7796), 568–571. https://doi.org/10.1038/s41586-020-2014-5

Wellner, J. (2022). ADCP (Hawaii UHDAS) data as collected during the cruise NBP2202, Thwaites and Dotson ice shelf. *Rolling Deck to Repository (R2R)*. [Dataset]. https://doi.org/10.7284/154856

Yang, H. W., Kim, T.-W., Dutrieux, P., Wåhlin, A. K., Jenkins, A., Ha, H. K., et al. (2022). Seasonal variability of ocean circulation near the Dotson Ice Shelf, Antarctica. *Nature Communications*, *13*(1), 1138. https://doi.org/10.1038/s41467-022-28751-5

Zheng, Y., Heywood, K. J., Webber, B. G. M., Stevens, D. P., Biddle, L. C., Boehme, L., & Loose, B. (2021). Winter seal-based observations reveal glacial meltwater surfacing in the southeastern Amundsen Sea. *Communications Earth and Environment*, *2*(1), 40. https://doi.org/10.1038/s43247-021-00111-z